INVESTIGATION OF THE AIR REFRACTIVITY EFFECTS ON IR SENSORS

IN THE MARINE BOUNDARY LAYER

D. Dion

B. Leclerc

Canada

INVESTIGATION OF THE AIR REFRACTIVITY EFFECTS ON IR SENSORS

IN THE MARINE BOUNDARY LAYER

by

D. Dion and B. Leclerc*

* Institut national d'optique

DEFENCE RESEARCH ESTABLISHMENT

CENTRE DE RECHERCHES POUR LA DÉFENSE

VALCARTIER

Tel.: (418) 844-4271

Québec, Canada   August/août 1990

SANS CLASSIFICATION

ABSTRACT

Refractivity effects in the marine boundary layer are investigated under representative conditions by using ray tracing. Effects on the variation of the maximum inter-vision range (optical horizon) and the angular error in relation to weather conditions are presented. The mirage formation is also analyzed. A parametric analysis shows that the contribution of water vapour to the total refractivity gradient is an order of magnitude lower than that of the temperature (in the IR spectrum regions free of significant resonances). For the analysis of refractivity phenomena, refractivity profiles are modelled to agree with the radio profiles defined in the NAAWS project. The influence of near-surface perturbations such as those caused by sea state and aerosols is assessed through simple tests. A brief analysis of meteorological statistics from two Atlantic regions provides indications about the occurrence of conditions that can produce noticeable effects on detection systems in relation to oceanic region and season.

RÉSUMÉ

A l'aide de la théorie des rayons (optique géométrique), on a étudié les effets de la réfringence atmosphérique dans la couche limite maritime dans des conditions représentatives. On présente des courbes analytiques montrant la variation de la distance maximale d'inter-vision (horizon optique) et l'erreur angulaire causées par la réfringence. La formation des mirages est aussi discutée. Une analyse paramétrique démontre que la contribution de la vapeur d'eau au gradient total de l'indice est inférieure d'au moins un ordre de grandeur à celle de la température dans les régions spectrales libres de fortes résonances. Pour une condition environnementale donnée, le profil de l'indice est modélisé de façon à être en accord avec le profil radio tel que défini dans le projet NAAWS pour cette même condition. L'influence des perturbations de surface, telles que celles causées par l'action des vagues et la présence d'aérosols, est analysée à l'aide de tests simples. Enfin, l'analyse de statistiques météorologiques dans deux régions de l'Atlantique nous renseigne sur la fréquence des conditions pouvant produire des effets notables sur les systèmes de détection en fonction de la région océanique et de la saison.

TABLE OF CONTENTS

1.0 INTRODUCTION

Air refractivity plays a major role in microwave propagation in the marine boundary layer. It is responsible for the formation of "ducts", which can trap energy well beyond the horizon, and anomalous fading zones depending on the conditions. Refractivity effects are of great concern to radar system analysts because they are known as the dominant propagation-related factor affecting radar detection performance.

Future ship sensor suites will be composed of IR and radar technologies. In the study of their complementarity, the issue of air refractivity effects in the IR has been raised because of their importance in radar propagation. So far, studies have been focussed on atmospheric absorption and aerosol extinction, as these are the main factors affecting IR detection, and the refractivity effects, which are known to produce a secondary effect, have never been thoroughly investigated.

The term "refractivity" refers to the real component of the air refractive index which determines the path of the radiation. By generating nonstraight-line radiation trajectories, the variation of air refractivity is expected to induce an angular error and affect the maximum inter-vision range (MIVR) (Ref. 1). The MIVR is an absolute maximum detection range. It is often wrongly called the "optical horizon" as opposed to the actual (or terrestrial) horizon which is, in this report, referred to as the "geometrical horizon". Air refractivity is also responsible for the multiple-image formation known as "mirage".

We have investigated these refractivity effects in relation to atmospheric conditions above the sea using ray tracing. First, we searched for an accurate expression that gives the air refractivity as a function of standard meteorological parameters (pressure, temperature and humidity), which is presented in Chapter 2.0. Using this expression, a parametric analysis was performed to assess the relative importance of water vapour and temperature on the total refractivity gradient, which determines the refractivity effects.

For the analysis of individual conditions, IR refractivity profiles were modelled on the basic principles of the marine boundary layer physics and they were made consistent with the radio refractivity profiles established in the NAAWS project. The profile modelling technique is described in Chapter 3.0.

Using ray tracing, a wide spectrum of refractivity conditions above the sea was analyzed. We considered the case of a sensor located 22 m above the mean sea level, which is typical of a shipborne surveillance system. The results are presented in Chapter 4.0. Theoretical predictions of the MIVR and the angular error in relation to weather conditions are shown. The mirage formation is also discussed. We have attempted to assess the effect of near-surface perturbations, such as those produced by aerosols or sea state, by incorporating thin hypothetical surface layers in which energy is totally extinct.

In Chapter 5.0, meteorological statistics are briefly analyzed to verify the occurrence of conditions that could produce noticeable refractivity effects in relation to oceanic region and season. Two North Atlantic regions are considered: CANLANT and Bermuda.

This work was initiated at DREV under PCN 32D05 during fall 1987 and was mainly carried out as a part of the Canadian contribution to the NAAWS project (Task DMCS 143) between August 1988 and January 1989.

2.0 EXPRESSION FOR AIR REFRACTIVITY IN THE IR

The electromagnetic properties of a medium are entirely defined by its index of refraction. This index is a complex number whose imaginary part indicates the energy absorption and whose real part indicates the phase velocity, which determines the radiation path. In this study, we investigate only the effects of the real component on IR detection. They are commonly called "refractivity effects".

For practical reasons, it is convenient to define the "refractivity" (N), in N-units, to represent the real component of the air refractive index, which is given by:

$$N = (n_r - 1) \times 10^6 \qquad [1]$$

where n_r is the real component of the index.

At microwave frequencies, air refractivity (N) can be obtained with good accuracy from standard meteorological parameters using the simple expression (Ref. 2):

$$N_{\mu w} = A \frac{P}{T} + B \frac{e}{T^2} \qquad [2]$$

where:

P: atmospheric pressure (mbar),

T: ambient temperature (Kelvin),

e: partial water vapour pressure (mbar),

A = 77.6,

B = 373 256.

The two additive terms in eq. 2 give the refractivity caused by the dry air constituents (oxygen, azote, etc.) and the contribution of water vapour, respectively.

Equation 2 is valid all through the radio bands where N does not vary significantly as a function of frequency. In the millimetric band, the anomalous dispersion caused by the 60-GHz water vapour resonance must be taken into account (Ref. 3). The anomalous dispersion expresses the abrupt variation of refractivity occurring at a significant gas resonance. As the frequency increases, atmospheric gas resonances become more and more frequent, which makes the evaluation of the refractivity more complex. Details on dispersion and on anomalous dispersion are given in Ref. 4 (pp. 105-110) and Ref. 5 (pp. 90-98).

In the IR, there is no widely used equation, such as eq. 2, to give the refractivity as a function of pressure, temperature and humidity. The difficulty is to derive a simple and accurate expression for the water vapour contribution as numerous resonances must be taken into account. For the last 30 years, the literature has provided formulae of increasing accuracy.

An expression for the refractivity of dry air is given by Goody (Ref. 6). Applying minor simplifications and using convenient units, Goody's expression can be rewritten under the simple form of the dry-air term of the radio refractivity expression. This yields:

$$N_{IR-dry} = \frac{A_{IR}(\lambda)\,P}{T} \qquad [3]$$

where P is the atmospheric pressure (in mbar) and T, the temperature (in Kelvin). $A_{IR}(\lambda)$ is given by:

$$A_{IR}(\lambda) = \frac{N_0(\lambda)}{3.518} \qquad [4]$$

where $N_0(\lambda)$ is known as "Edlén's formula" which gives, for λ expressed in μm, the air refractivity at normal pressure, 15^oC and for a CO_2 concentration of 0.03% (Ref. 7):

$$N_0(\lambda) = 64.328 + \frac{29498.1}{146 - \frac{1}{\lambda^2}} + \frac{255.4}{41 - \frac{1}{\lambda^2}} . \qquad [5]$$

According to Goody (Ref. 6), eq. 3 would be valid from 0.2 to 20 μm and would thus encompass both the visible and the IR spectra. It is worth noting that the variation of N_{IR-dry} versus λ is very weak in the IR spectrum.

Equation 3 gives the air refractivity in the absence of water vapour (i.e. 0% relative humidity). The calculation of the water vapour contribution at optical wavelengths is discussed by Hill et al. (Ref. 9). They emphasize that in order to achieve a valid calculation in the IR, a sum of all spectral lines' dispersion has to be performed over the whole electromagnetic spectrum. Hill and Lawrence (Ref. 10), have quite recently published a

simple formula that was obtained by the integration of the contribution of more than 40 000 spectral lines. Using the form of the second term of eq. 2, it can be written as:

$$N_{IR-WV} = \frac{216.5\ e}{T}\ \zeta(\lambda,T) \qquad [6]$$

where **e** expresses the water vapour pressure (in mbar) and:

$$\zeta(\lambda,T) = \frac{0.957 - 0.928\ (\chi-1)\ \tau^{0.4}}{1.03\tau^{0.17} - 19.8\chi^2 + 8.2\chi^4 + 1.7\chi^8} + \frac{3747}{12440 - \chi^2} \qquad [7]$$

where:

$\chi = 10/\lambda$,

$\tau = T/273.16$,

T: temperature (Kelvin),

λ: wavelength (μm).

The computation of water vapour refractivity was performed for wavelengths between 7.8 and 19 μm and the fitted formula (eq. 7) was *a posteriori* weighted slightly to agree with measurements made near 10.6 μm. The formula is also considered valid in the 3-5 μm window. The agreement between calculated and measured refractivity near 3.5 μm is shown in Ref. 10.

As pointed out by the authors, when calculating water vapour refractivity with a strong resonance nearby, the associated anomalous dispersion should be added to eq. 6 since it may significantly contribute to the total refractivity (see Ref. 10). However, such a resonance also causes absorption which has a greater effect in the IR. For the study of refractivity effects, we think that these anomalous dispersions can be ignored (at least in

first analysis), assuming that, in the IR, the generated absorption will overcome any refractivity effects.

Total refractivity can then be obtained using eq. 6 in conjunction with eq. 3. One must subtract from eq. 3 the portion of water vapour pressure included in the total atmospheric pressure P. Hence, the expression for the total air refractivity in the IR can be written as:

$$N_{IR} = \frac{A_{IR}(\lambda)\, P}{T} + \frac{e}{T}\Big[216.5\ \zeta(\lambda,T) - A_{IR}(\lambda)\Big]\ . \qquad [8]$$

In fact, the refractivity of dry air is greater than that of water vapour (at least in the region free of significant H_2O resonances) and thereby, for a given volume of air, the presence of water vapour will produce a negative contribution to the total refractivity.

For the refractivity effect analysis presented in this report, a single wavelength of 10 μm is considered. Equation 6 has been specifically validated in the vicinity of this wavelength. The results obtained at this central wavelength should be representative of the refractivity effects in the whole 8-12 μm window since this window is fairly clean of resonances.

Refractivity effects are not related to the refractivity itself but rather to its gradient. In the troposphere, the refractivity gradient can be reduced to its vertical variation. Thus, a simple parametric analysis may help show the relative importance of temperature and water vapour. The variation of N as a function of the elevation is given by:

$$\frac{dN}{dh} = \frac{\partial N}{\partial P}\frac{dP}{dh} + \frac{\partial N}{\partial T}\frac{dT}{dh} + \frac{\partial N}{\partial e}\frac{de}{dh} \qquad [9]$$

which shows that the gradient of N is a function of P, T, e and their derivative with respect to the elevation.

Figures 1 and 2 show respectively the refractivity gradient versus the temperature gradient and the water vapour pressure gradient. In this example, the atmospheric pressure is 1013 mbar at the surface and it decreases at a rate of 0.12 mbar/m and, the ambient relative humidity is 85%. The graphs show that the contribution of water vapour is an order of magnitude lower than that of temperature.

Unlike in the microwave spectrum, where the water vapour density is primarily responsible for the refractivity phenomena (ducting, subrefractivity, etc.), this result indicates that water vapour plays a secondary role in the IR. In a first approximation, it could be ignored; NOSC did so in their analysis (Ref. 1). It has nonetheless been incorporated into our analysis.

3.0 MODELLING OF THE REFRACTIVITY PROFILES

To achieve a valid analysis of refractivity effects, one needs a detailed knowledge of air refractivity in the region where energy propagates. This requires a high-precision measurement of the relevant meteorological parameters, which proves to be very tricky or even unachievable. Many scientists even question the reliability of the fine measurement of profiles. An usual approach is to rely on atmospheric models that used a reduced set of
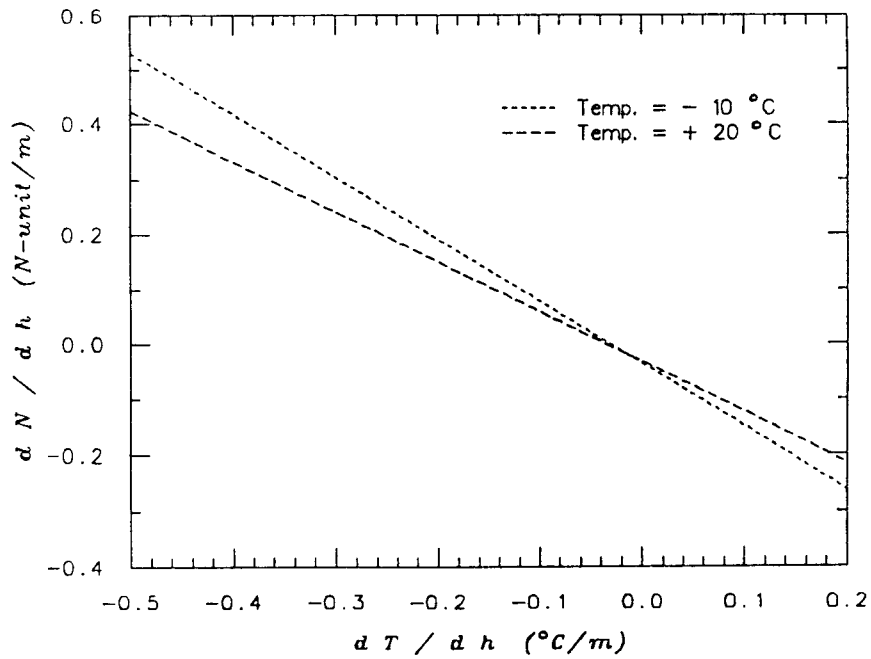
FIGURE 1 - Total refractivity gradient versus temperature gradient;
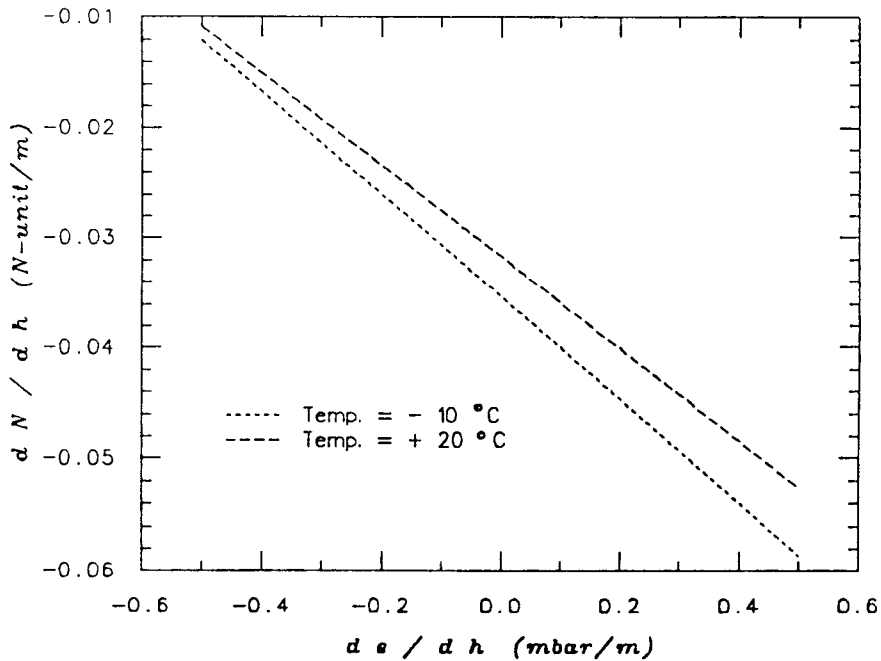de/dh = 0, dP/dh = -0.12 mbar/m; RH = 85%, P = 1013 mbar

FIGURE 2 - Total refractivity gradient versus water vapour pressure gradient;
dT/dh = 0, dP/dh = -0.12 mbar/m; RH = 85%, P = 1013 mbar

meteorological parameters. Another advantage of this approach is that it facilitates the generalization of results obtained from the analysis of individual cases. It must be kept in mind that the lack of knowledge on the propagation medium constitutes the main source of uncertainty in the analysis of tropospheric refractivity effects; the validity and accuracy of the propagation models used are adequate.

An assumption usually made in this type of analysis is to consider the atmosphere as being horizontally homogeneous. This reduces the characterization of air refractivity to a vertical profile. This assumption should normally be valid in an open sea environment. However, in some conditions, air refractivity could notably vary horizontally (mainly in the IR), which could significantly effect many results presented in this report. The impact of this assumption is discussed in Chapter 6.0.

The marine boundary layer physics provide models to describe the vertical structure of the atmosphere above water. In particular, models were developed to determine the radio refractivity profiles under evaporation-duct conditions from only four meteorological measurements (called bulk measurements): air temperature, humidity and wind speed at a reference height and sea temperature (Refs. 14 and 15). The advantage of this technique is that it requires a reduced set of common meteorological parameters that are part of a standard weather sounding routine (as performed by weather ships).

NOSC used that approach to derive radio refractivity profiles (Ref. 14); their profiles were adopted in the framework of the NAAWS project for the radar performance analyses. A particularity of the NOSC profile derivation is that the air stability effect is not fully taken into account in the function modelling. It is, however, included in the

calculation of the duct height which is the main profile characteristic; given an environmental condition, an associated radio duct height is evaluated from the bulk measurements (Refs. 14 and 15).

In order to consider IR refractivity profiles that are consistent with the NAAWS radio profiles, the profiles used in our analysis were modelled as follows.

Atmospheric pressure is assumed to vary linearly with respect to the elevation as:

$$P(h) = P_0 - 0.12 \, h \qquad\qquad [10]$$

where P_0 is the surface pressure (expressed in mbar) and h is in metres. A similar model was adopted by GEC-Marconi Ltd. in their refractivity analysis (Ref. 8).

Temperature variation is described by the characteristic logarithmic function of neutral (or near-neutral) atmospheric conditions (Ref. 13):

$$T(h) = T_0 + \Gamma_r (T_r - T_0) \ln\left(\frac{h+z_0}{z_0}\right) . \qquad\qquad [11]$$

Note that this function does not include the integrated Monin-Obukhov function term to account for stability (as done in Ref. 8). T_r is the air temperature at a reference level and T_0 is the temperature at the surface, which corresponds to sea temperature. Γ_r is a constant of proportionality given by:

$$\Gamma_r = \frac{1}{\ln[\,(z_r + z_0)/z_0\,]} . \qquad\qquad [12]$$

The reference height z_r is commonly set to 6 m in the calculations although the actual level of measurement is usually much higher (about 12 m in the case of weather ships); this may cause an error in the function modelling. z_0 is called the surface roughness parameter, which refers to the hydrodynamic character of the surface and not to the wave motion or the sea state. In the analyses, the average value of 1.5×10^{-4} m is commonly used (Ref. 15). As z_0 may be significantly different under certain conditions (Ref. 16), its inaccuracy may be another source of error.

Lastly, knowing P and T, the water vapour pressure e is obtained from the radio refractivity profile given in Ref. 14 (knowing the radio duct height) using the expression of radio refractivity (eq. 2).

The P, T and e vertical profiles thus obtained have proved to be in good agreement with most of the estimated profiles given in Ref. 17.

The P, T and e profiles are used in eq. 8 to give the refractivity profile in the IR. Using this technique, we obtain for a weather condition under analysis, a refractivity profile in the IR that is based on assumptions similar to those made for the NAAWS radio profiles in terms of air stability and humidity profile.

Since air refractivity in the IR mainly depends on temperature, the temperature expression (eq. 2) turns out to be the most sensitive. The main sources of error are, as noted above, the cancellation of the Monin-Obukhov stability function and the inaccuracies on z_0 and Γ_r. Nonetheless, the model used here is considered sufficiently adequate and representative for a first investigation of the refractivity effects. However, to obtain more

accurate predictions of the refractivity effects, particularly when considering individual cases, one should use more accurate profiles, emphasizing the temperature profile.

4.0 RAY-TRACING ANALYSIS

The speed of radiating energy in a medium obeys the law v=c/n, where n is the refractive index characterizing the medium and c the speed of light in free space. Taking the example of an isotropic plane wave, one can demonstrate that for a nonhomogeneous medium, the speed of the wave will vary along the wavefront, which will modify its orientation and may bend it. Knowing the medium's index, the path of the radiation in any given direction can be determined by the geometrical optics which describes the propagation of energy by means of rays. Its validity in relation to the classical electromagnetic Maxwell's theory is discussed in Refs. 7, 20 and 21.

When the low troposphere is considered horizontally stratified (horizontally homogeneous) and the beam of energy is nearly horizontal, it can be shown that the curvature of a ray varies as (Ref. 20, pp. 41-58):

$$\frac{1}{\rho} = -\frac{dn}{dh} \qquad [13]$$

where ρ is the radius of curvature, n the refractive index and h the height above the surface.

If a linearly varying atmosphere is considered (dn/dh constant), eq. 13 indicates that the curvature of rays remains constant and thereby the geometry is simplified so that the

investigation of refractivity effects can be carried out analytically. Although it is shown in Chapter 3.0 that in the marine boundary layer, the case of interest, refractivity varies rather logarithmically, the use of this hypothetical atmospheric model helps introduce refractivity phenomena. Furthermore, the results obtained from this model are a useful reference for more detailed analyses.

4.1 Analysis Considering a Constant Refractivity Gradient

The common technique to account for the earth's curvature in tropospheric refractivity analysis is to modify the vertical refractivity profile so that the earth may be considered flat. This leads to the concept of a modified index of refraction (m) which is related to n by:

$$m(h) = n(h) + \frac{h}{a} \tag{14}$$

where a is the earth's radius and h is the height normal to the sea surface. Then, in a flat earth representation, the ray curvature will be given by:

$$\rho = -\frac{1}{\frac{dm}{dh}} . \tag{15}$$

As dm/dh mainly depends on the temperature gradient, we will examine the effects produced while varying the temperature gradient only. The atmospheric pressure and the partial water vapour pressure will be considered as decreasing linearly at a rate of 0.12 mbar/m and 0.1 mbar/m, respectively. For $P_0 = 1013$ mbar, $T_r = 12$ °C and a relative humidity of 85%, we obtain the following relation between dm/dh and dT/dh:

$$\frac{dm}{dh} = (0.132 - 0.963 \frac{dT}{dh}) \times 10^{-6} \ . \tag{16}$$

For dT/dh constant (= $\Delta T/\Delta h$), dm/dh is constant and the rays are regular arcs with a radius ρ (see eq. 15). For a ray identified by its initial direction angle (launching angle) θ defined from the horizontal, the ray path is described in cartesian coordinates by the equation:

$$(x - \rho \ \sin\theta)^2 + (y - h_s - \rho \ \cos\theta)^2 = \rho^2 \tag{17}$$

where h_s is the sensor height above sea level.

Varying $\Delta T/\Delta h$, the magnitude of the temperature gradient, we note two refractivity phenomena: (1) a varying maximum inter-vision range (MIVR), which is an absolute limit of the detection range, and (2) an angular error.

In an homogeneous atmosphere (dn/dh = 0), the rays are simply straight lines in a spherical earth representation and the MIVR corresponds to the terrestrial horizon. When dn/dh is positive (dT/dh negative), the rays are bent upward with a curvature proportional to $|dT/dh|$, decreasing the MIVR. This condition is known as subrefractive. When dn/dh is negative (dT/dh positive), the rays are bent downward, extending the MIVR beyond the horizon. This condition is known as super-refractive.

The ray that goes the farthest is the one that is tangent to the earth's surface. By a simple algebraic development, one finds that this ray is given by:

$$\theta_{hor} = - \arccos\left(\frac{\rho + h_s}{\rho}\right) .$$ [18]

The MIVR depends on target height. For an inbound target flying at a constant altitude h_t, the MIVR can be obtained using eq. 17 in conjunction with eq. 18, which yields:

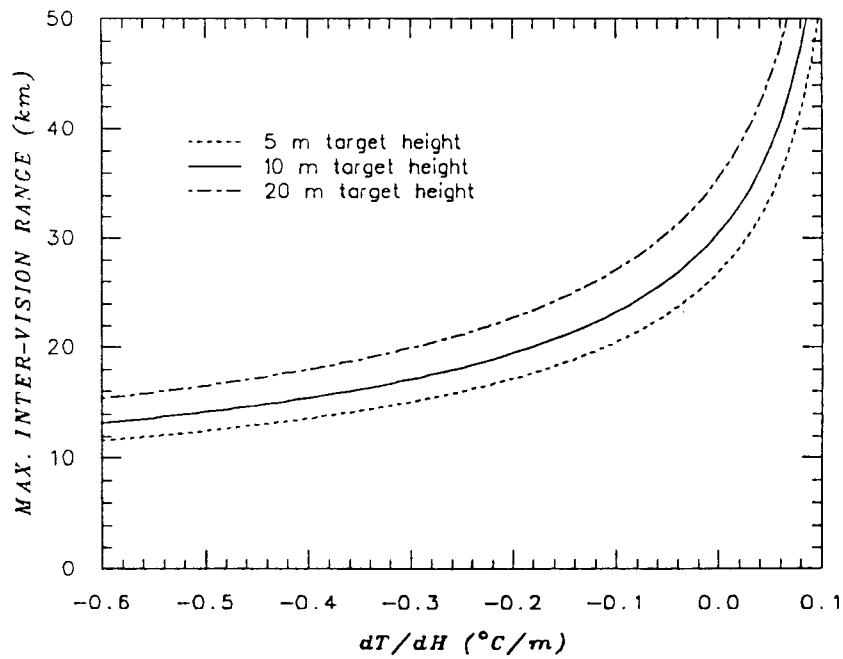$$MIVR = \sqrt{\rho^2 - \left(h_t - h_s + \rho \cos\theta_{hor}\right)^2} + \rho \sin\theta_{hor} .$$ [19]

FIGURE 3 - Maximum inter-vision range versus temperature gradient for a linearly
varying atmosphere

Figure 3 shows MIVR versus dT/dh for a sensor located 22 m above the sea surface and for three target heights: 5, 10 and 20 m. The curves show a significant variation of the MIVR with respect to dT/dh ($\Delta T/\Delta h$). For large negative temperature gradients, the MIVR can be as low as 12 km for the 5-m target, which represents a reduction or a loss of about 18 km with respect to the horizon. For higher targets, theMIVR is greater as expected. We note that the greatest variation of MIVR occurs when dT/dh ($\Delta T/\Delta h$) varies slightly around zero, while for large negative values of dT/dh the MIVR decreases more slowly; the 5-m target curve shows a reduction of 7 km when dT/dh goes from 0.0 to -0.1 $^{\circ}$C/m. For positive temperature gradients, the graph shows a rapid increase of the MIVR, which leads to astonishing ranges. However, as will be discussed further, a positive temperature gradient is likely to increase evaporation at the sea surface. This could decrease or even nullify the potential MIVR extension due to water vapour extinction which is a dominant factor in the IR.

The curvature of rays will cause an error of positioning as exhibited in Fig. 4. Using the equation of a ray (eq. 17), we can calculate the required launching angle to hit a target position (r_t,h_t) for a given dm/dh. By isolating θ in eq. 17, we obtain:

$$\theta = \arcsin\left(\frac{\sqrt{r_t^2 + (h_s - h_t)^2}}{2\rho}\right) - \arccos\left(\frac{r_t}{\sqrt{r_t^2 + (h_s - h_t)^2}}\right) . \qquad [20]$$

We define the angular error as the difference between this angle and the one that would be obtained in an homogeneous condition (dn/dh = 0). Still considering a constant-altitude inbound target, we calculate the angular error at the MIVR (i.e. when the sensor begins to "see" the target). It is given by:
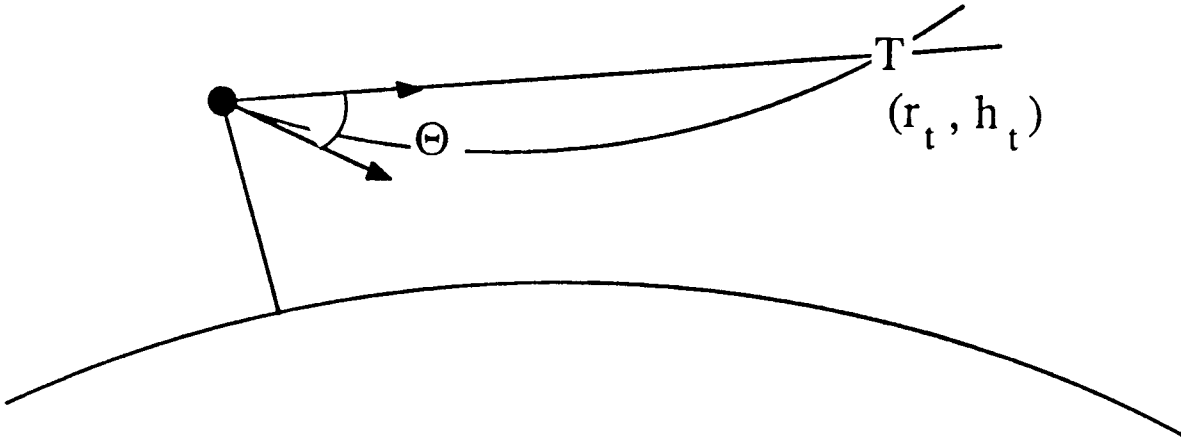
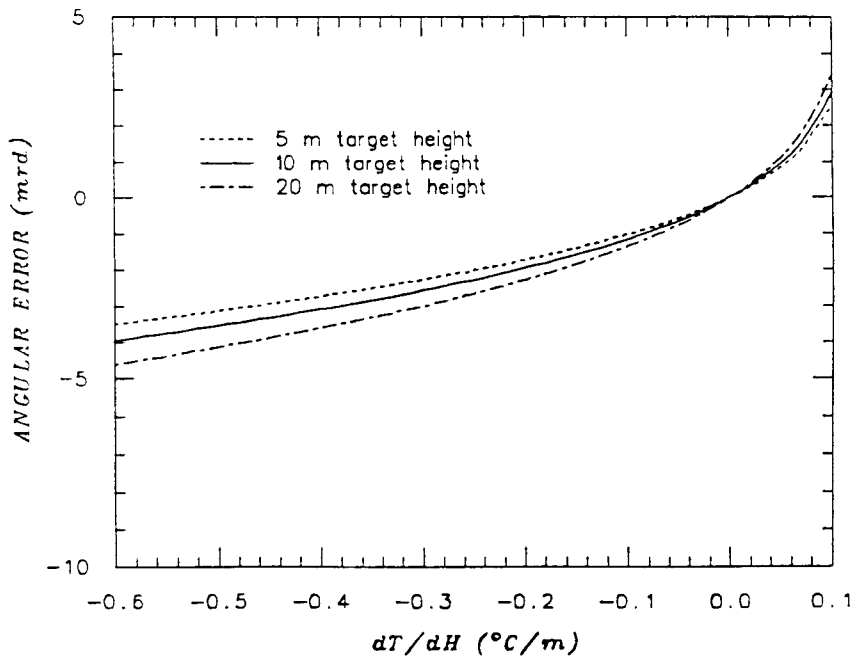FIGURE 4 - Angular error induced by the curvature of the rays

FIGURE 5 - Angular error versus temperature gradient for a linearly varying atmosphere

$$\Delta\theta \;=\; \theta(MIVR, h_t) \;-\; \theta(MIVR, h_t)\Big|_{\frac{dT}{dh}=0} \qquad\qquad [21]$$

where MIVR is obtained by using eq. 19.

Figure 5 shows the angular error versus dT/dh for the three target heights (5, 10 and 20 m). The graph indicates that the angular error reaches about 5 mrad at high temperature gradients.

4.2 Analysis Using Logarithmic Refractivity Profiles

As stated in Chapter 3.0, in the marine boundary layer, air refractivity does not vary linearly but rather logarithmically. Figure 6 shows two examples of refractivity profiles obtained by following the approach described in Chapter 3.0: one presents a strong subrefractivity condition and the other, a super-refractivity condition. A noticeable characteristic of these profiles is that refractivity mostly varies in a very thin layer at the surface, a couple of metres at most, where very strong gradients are encountered.

To perform refractivity analysis under specific weather conditions, computer programs were developed (1) to model the IR refractivity profiles (based on the method described in Chapter 3.0) and (2) to produce the ray-tracing diagrams and evaluate the MIVR and the angular error.

The ray-tracing diagrams obtained in the case of the two refractivity profiles presented in Fig. 6 are shown in Figs. 7 and 8, respectively. Both the flat and curved earth representations are shown. Although the curved-earth diagrams are technically less convenient, the effects on the MIVR may be more evident. The presented ray-tracing
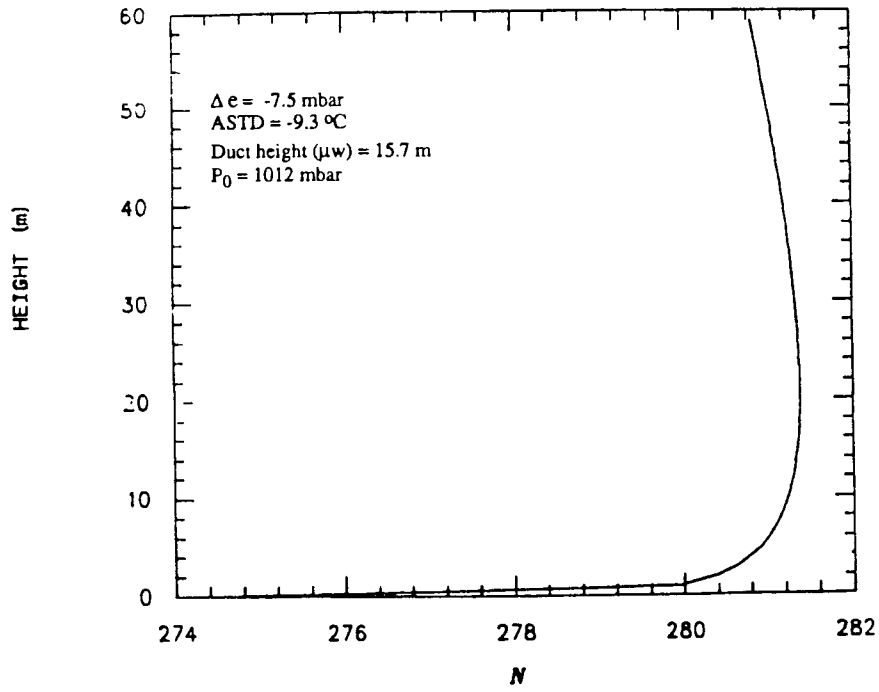
FIGURE 6a - Example of a refractivity profile under a subrefractive condition
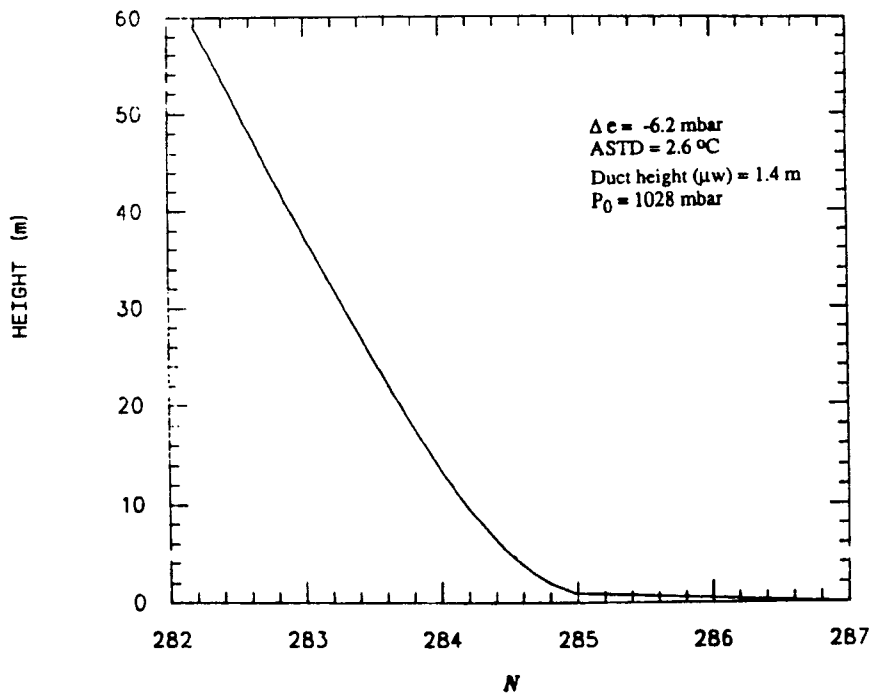

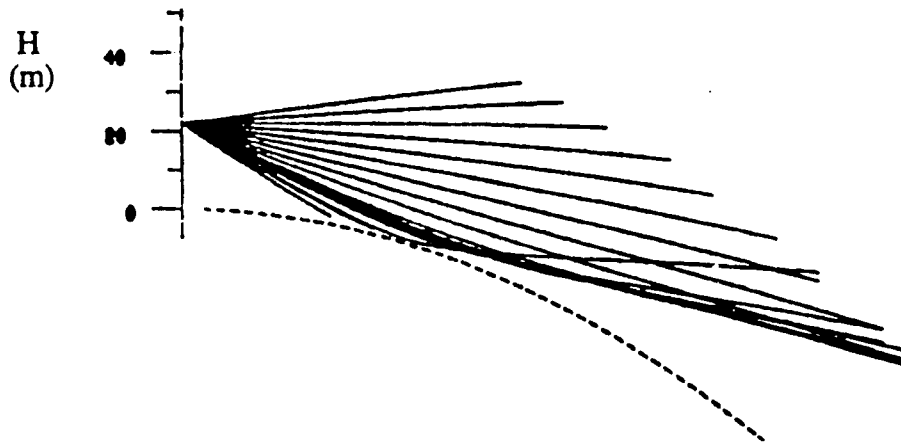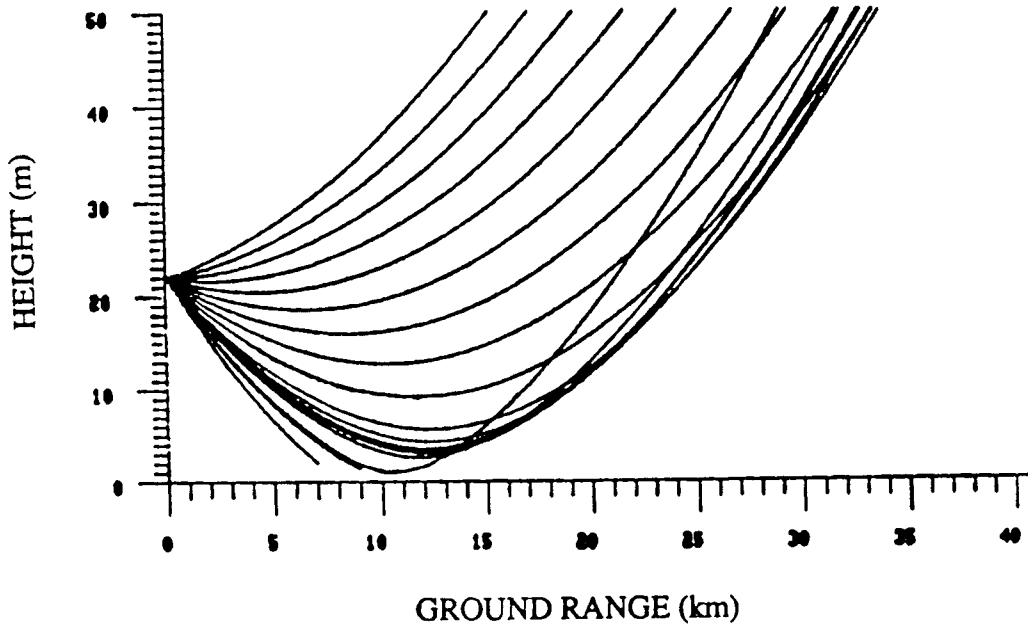FIGURE 6b - Example of a refractivity profile under a super-refractive condition

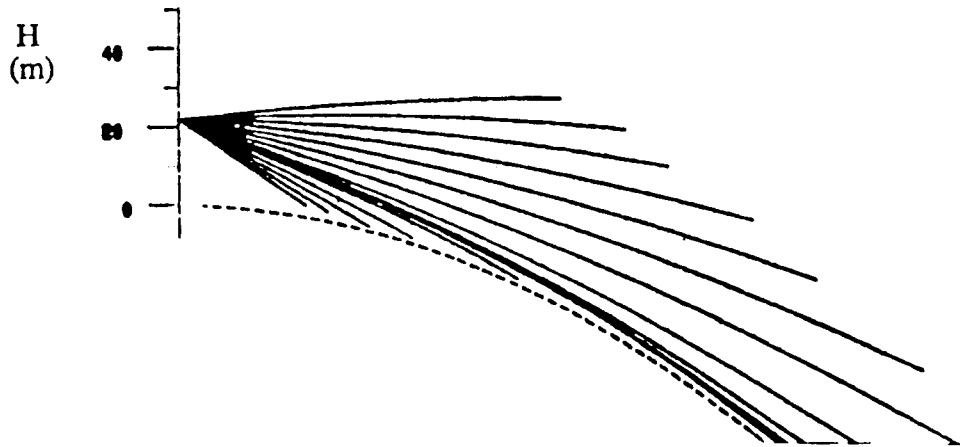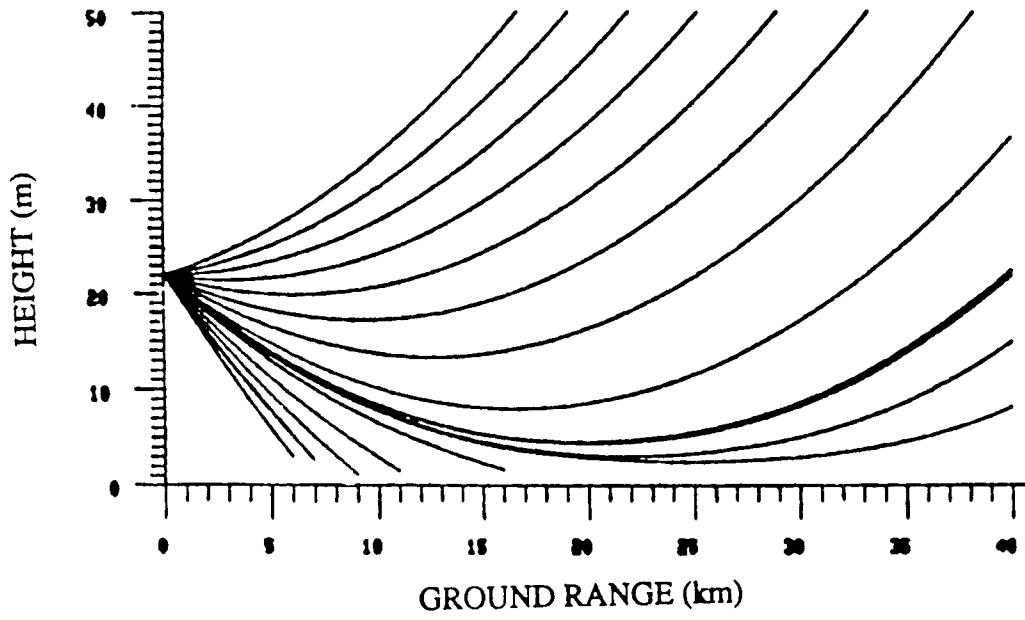FIGURE 7 - Ray-tracing diagram generated using the refractivity profile of Fig. 6a

FIGURE 8 - Ray-tracing diagram generated using the refractivity profile of Fig. 6b

diagrams are made of evenly spaced rays with a 0.15° interval. In addition, they include the rays that hit the three targets at their respective MIVRs. These rays were obtained by interpolation with a precision of about 0.0015°.

In a thin layer adjacent to the surface, the propagation is likely to be degraded by the absorption and scattering caused by surface aerosols. Furthermore, although the actual effect of waves on a refractivity profile is not known, it is not unreasonable to believe that the wave motion could highly perturb the assumed static profile and, also, could possibly "wash out" a bottom portion of the profile, as contended in Ref. 8. In the computation, rays are stopped 1 m above the surface; this is apparent on the flat-earth diagrams. We deemed it more realistic to neglect, throughout the analysis, the rays that represent energy likely to be highly absorbed due to these near-surface phenomena. By doing so, we reject the effects that would rely on energy that skims the earth very closely. This layer, within which we assume that no energy propagates (here arbitrary made equal to 1 m), will be called the "absorbing surface layer" in this report.

Since the vertical temperature variation is the dominant factor affecting air refractivity in the IR, as shown in Chapter 2.0, it is convenient to use the standard air-sea temperature difference (ASTD) measurement to characterize a given meteorological condition under analysis. Note that ASTD (or $T_r - T_0$) is the basic parameter of our temperature profile model (eq. 11). Thus, the magnitude of the refractivity effects can be presented as a function of ASTD. ASTD is obviously dependent upon the reference height (the height at which air temperature is measured). One must then ensure that the reference height is common when comparing various environmental conditions. In this study, we used ASTDs such as those measured by ocean weather ships.

The ray-tracing analysis was performed using NAAWS representative weather profiles (Ref. 21) covering a wide spectrum of refractivity conditions; ASTD cases ranging from -8 to +4 were considered. The dot-graph of Fig. 9 shows the MIVRs (versus ASTD) obtained for the 5-m target. The same exercise was repeated for the 10- and 15-m target heights and curves were fitted to the discrete results to produce prediction curves.

The resulting MIVR curves are plotted in Fig. 10. Negative ASTD conditions are meteorologically called unstable, and oppositely, positive ASTD conditions are called stable. The graph shows that, under very unstable conditions, the reduction of the MIVR may reach 10 km. It is interesting to note that the difference between these predictions, for negative ASTDs, and those considering a constant temperature gradient (Fig. 3) is not very significant. A difference of less than a couple of kilometres is observed. This would indicate that, under unstable conditions, the MIVR is not very dependent upon the refractivity profile model. The results for positive ASTDs (stable conditions) are, however, significantly different showing ranges that increase much less rapidly. This is in part due to the cancellation of rays in the absorbing surface layer.

Important information can be extracted from the variation of radiation intensity (which is related to the power density) since it directly affects detection. In a ray-tracing diagram, the intensity is exhibited by the convergence or the divergence of rays. The variation of intensity along rays can be determined by measuring the spacing between adjacent rays through an algorithmic process. A rigorous calculation is now contained in modern ray-tracing techniques (Ref. 22). Although, we did not carry out extensive intensity computations, simple tests showed that when the MIVR is greater than the

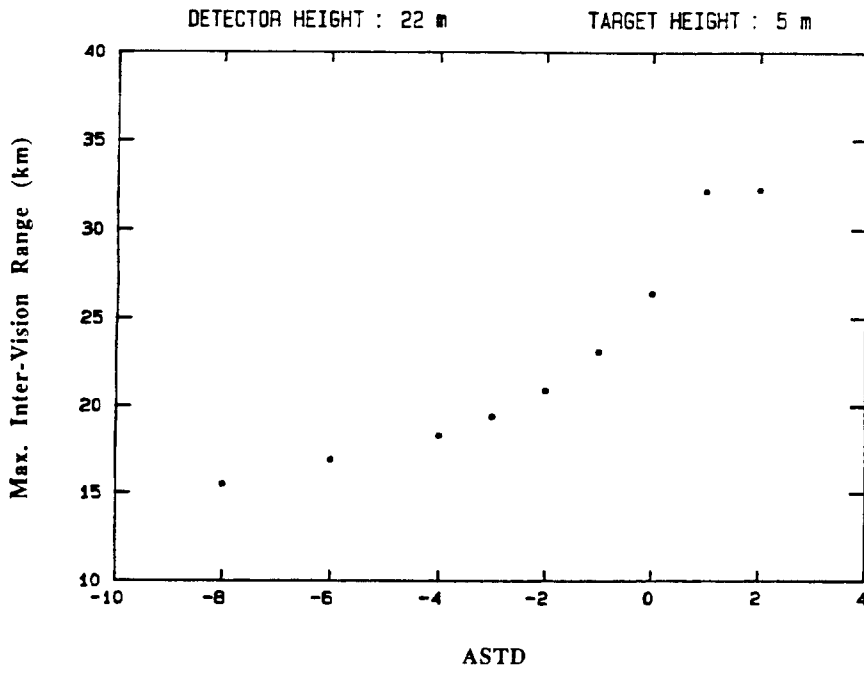DETECTOR HEIGHT : 22 m   TARGET HEIGHT : 5 m

FIGURE 9 - MIVRs obtained for the considered conditions
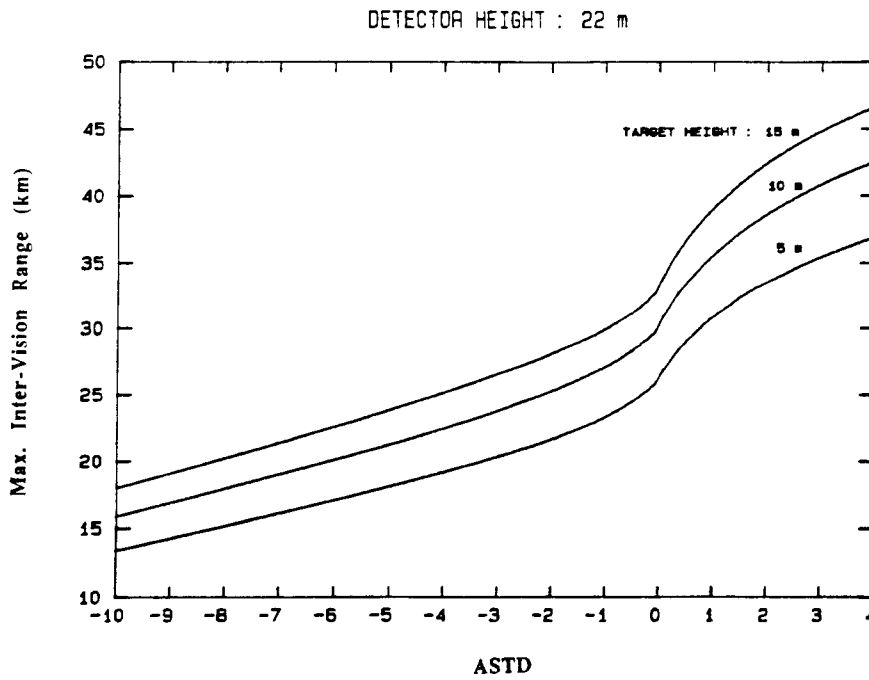
DETECTOR HEIGHT : 22 m

FIGURE 10 - MIVR prediction curves for inbound targets flying at a constant altitude of 5, 10 and 15 m above sea level

horizon, near the horizon and beyond, the intensity decreases much more rapidly than in $1/r^2$. Therefore, the detection range could be much lower than the predicted MIVR. Under subrefractive conditions, where the MIVR is shortened, the intensity of the radiation progressively departs from its $1/r^2$ variation at about mid-course to theoretically increase very strongly near the MIVR. In fact, as shown in the ray-tracing diagram of Fig. 7, a caustic is formed at the MIVR. Consequently, although the MIVR is shortened, detectability should be improved near the MIVR.

As an indication on the importance of the surface perturbations in the refractivity mechanisms, Fig. 11 gives, for various conditions (dots), the closest point to the earth (or the lowest point) of the ray that reaches the 5-m target at the MIVR; straight lines were fitted to provide an estimate for any ASTD. The graph shows that for an ASTD greater than $3°C$ (3<ASTD<-3), that ray does not go below 3 m. This indicates that under strong refractivity conditions, the refractivity effects would not be very dependent upon what happens in the first 3 m (assuming, of course, that the refractivity profile above 3 m is unaffected by perturbations occurring below 3 m). For an ASTD lower than $3°C$, however, the ray that determines the MIVR has to go closer to the earth. Under these conditions, the potential refractivity effects would be more dependent on the near-surface perturbations. Since weak effects are expected in these conditions, the surface perturbations could virtually nullify them.

The angular error versus ASTD obtained for the three targets at the MIVR is plotted in Fig. 12. We observe a weak angular error in comparison with the results obtained considering a constant temperature gradient. Under unstable conditions (negative ASTD), the error does not exceed 1 mrad even under extreme conditions as opposed to errors of the
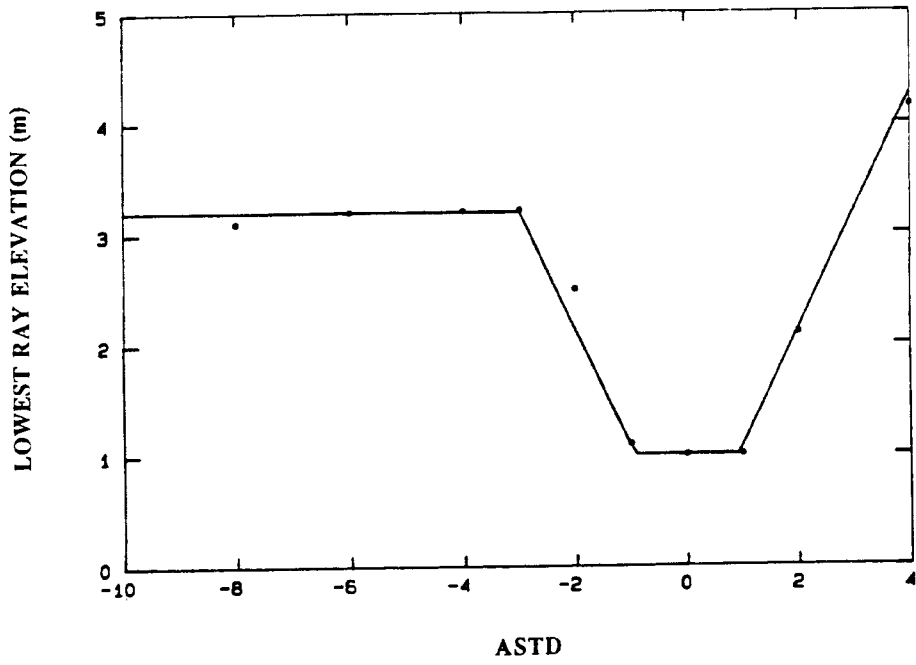
FIGURE 11 - Lowest point of the ray that reaches the 5-m target at the MIVR
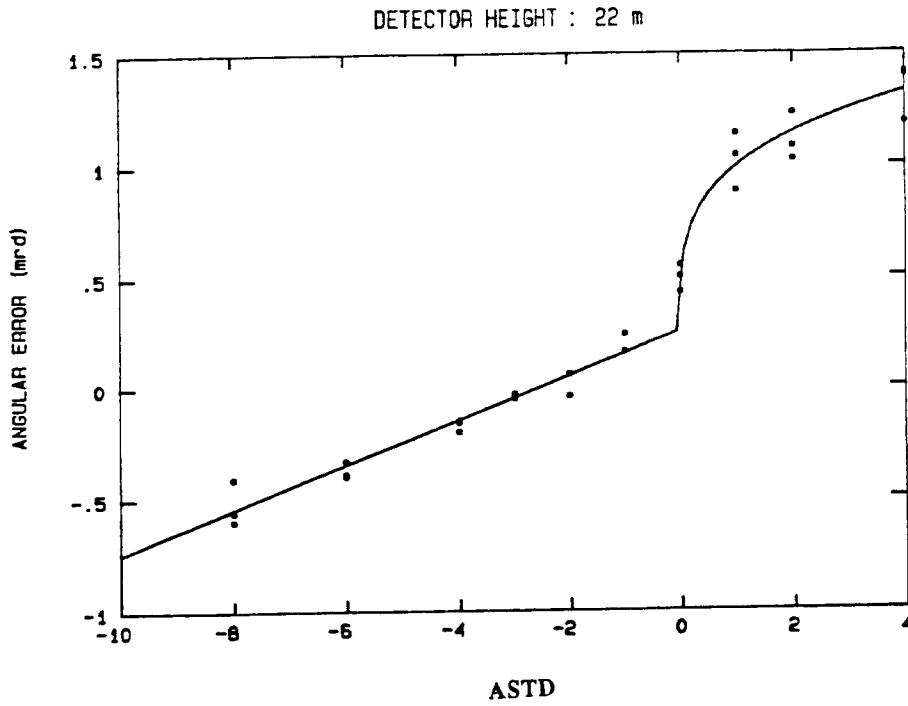
DETECTOR HEIGHT : 22 m

FIGURE 12 - Angular error obtained at the MIVR for low-altitude inbound targets

order of 5 mrad obtained considering constant temperature gradients (Fig. 5). Under stable conditions (positive ASTD), slightly higher values are obtained.

Since a varying-gradient profile generates rays of varying curvatures, it can produce ray crossing. Thus, depending on the conditions, a point target may be hit by more than one ray, which means that the object is seen in different directions at the same time. This multiple-image formation is known as "mirage". As shown in Fig. 13, under subrefractivity conditions (unstable conditions), the use of a logarithmic profile creates a mirage zone where a point-target is reached by more than one ray. In the figure, the energy striking Point M comes from two different directions and this turns out to be the case for any point in the defined mirage zone except very near the MIVR where more rays collide to form a caustic. Actually, one expects that a caustic as sharp as those obtained theoretically is not likely to occur because of the neglected atmospheric fluctuations along the radiation path. Furthermore, as shown in Fig. 13, should it be present, the caustic would impact on the detection of a constant-altitude target only over a very short range. In the case of Fig. 13, when a double-image formation occurs, we note that the lowest ray involved skims the earth in such a way that the lower image may appear as a reflection; this is more evident in the curved-earth diagram of Fig. 7. Thus, in practice, it could be difficult to discriminate between a reflection and a refractivity effect; this was already experienced during field trials with a 10.6 μm laser source.

In the ray-tracing diagram of Fig. 13, we note that the width of the mirage zone increases as a function of elevation. In this case, for instance, a constant-altitude target flying at 15 m would cross a 3-km mirage zone when a target at 5 m would encounter a 1-km mirage zone. Figure 14 shows, for a target flying at 15 m, the limits of the mirage
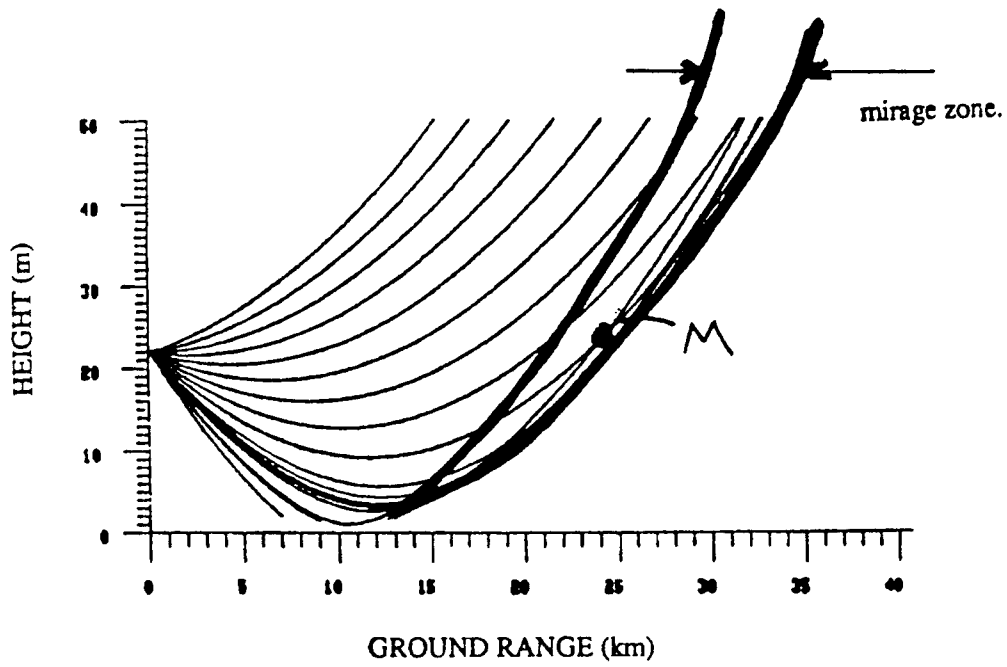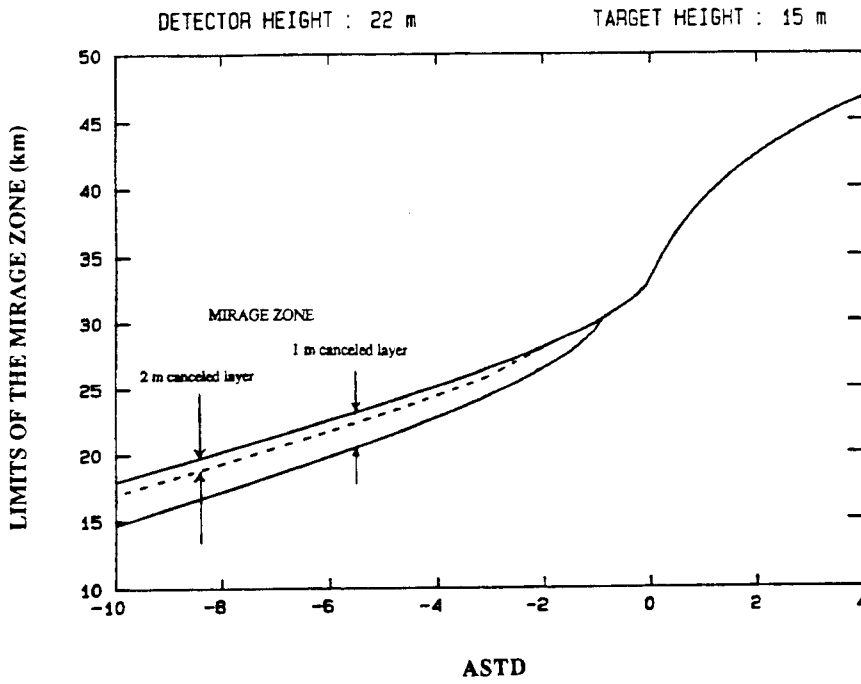
FIGURE 13 - The mirage zone

FIGURE 14 - Limits of the mirage zone with respect to ASTD

zone (and indirectly its width) in relation to the degree of subrefractivity expressed by ASTD; the superior curve is the MIVR curve shown in Fig. 10. The graph shows that a mirage zone is present when ASTD < -1 and that its width does not appreciably vary with respect to ASTD. The dashed curve indicates the new limit of the mirage zone that is obtained when considering a 2-m absorbing surface layer instead of a 1-m layer. This gives indications about the vulnerability of the mirage to perturbations in a thin surface layer. In this case, we notice that the mirage zone is significantly reduced. This could be expected since, as observed above, the lowest ray that hits the target (the one responsible for the double-image formation) has to skim the earth very closely.

When a mirage occurs, the separation between the two images can be described as the angle between the two rays hitting the target. One can observe that this angle is greater for an elevated target and increases as the target gets closer to the platform. At an elevation of 15 m, a maximum separation angle of about 1 mrad is measured in the case of the ray-tracing diagram of Fig. 7 (or Fig. 13) which represents a fairly strong sub-refractivity condition. This separation angle is not likely to create clearly separate images in the case of real targets. This may rather result in a significant distortion (stretching) of the expected image. An example of such a phenomenon is shown in Ref. 1.

5.0 OCCURRENCE ANALYSIS

In the previous chapter, we presented and discussed the refractivity effects under meteorological conditions, which were characterized by the air-sea temperature difference (ASTD). To assess the actual importance of refractivity on sensor performance, one must

examine the statistical behaviour of ASTD, with respect to the time of year and the oceanic region, to verify the occurrence of conditions that may potentially produce significant effects on sensors.

An environmental data base is being developed at DREV to support EO and radar sensor performance analyses. The main feature of the data base is that, for a given region, the meteorological data are presented in relation to the dominant air masses for all seasons; in general, four to five air masses are considered per season. The occurrence of air masses is given by season and statistics about ASTD are provided for the different air masses. It is interesting to note that there is a strong correlation between ASTD distributions and types of air mass; this is also noted for the evaporation-duct height distributions. Using the available ASTD histograms together with the prediction curves provided in Chapter 4.0, the importance of air refractivity on IR detection can be assessed in relation to oceanic regions.

In the following analysis, the CANLANT and Bermuda regions have been selected for comparison. They present very different ASTD statistics and provide a wide range of ASTD conditions; in the North Atlantic, the ASTD statistics vary considerably depending on the subregions, more specifically from north to south.

For the Bermuda region, Fig. 15 shows simplified winter and summer ASTD histograms which account for 90% of the events. The data are from weather ship ECHO. We can note that ASTD is fairly low most of the time during summer; it remains between -2 and +1°C 90% of the time. During winter, higher negative ASTDs are encountered but they seldom go below -4 (only 5% of the time). In either season, positive ASTDs (stable conditions) are very rare. Consequently, for this region, according to the prediction curves

developed in Chapter 4, significant effects caused by air refractivity can be virtually discarded. The loss in MIVR should not exceed a few kilometres, the angular error should be less than 0.2 mrad and the presence of mirage is very improbable. Furthermore, according to Fig. 11, a major influence of the near-surface perturbation is expected, which should tend to overcome any refractivity effects.

For the CANLANT zone, data from two subregions are considered: Labrador Basin and Newfoundland Basin. The ASTDs recorded during winter in the Labrador Basin (weather ship BRAVO) are shown in Fig. 16. The figure shows ASTD distributions grouped by air mass. This emphasizes the strong relationship between the behaviour of ASTD and the air mass breakdown. Each air mass box contains 90% of the recorded ASTDs for that air mass. An astonishingly high occurrence of very unstable conditions is noticed; global winter statistics (not presented here) indicate that 30% of the time ASTD is greater than -6, and 15 % of the time it is greater than -8 °C. According to the predictions obtained in Chapter 4.0, such large negative ASTDs would lead to a MIVR reduction of 5 to 10 km and an angular error of 1 mrad or more. Furthermore, depending on the near-surface perturbations and sea state, there is a possibility of mirage over a few kilometres.

Moving slightly south, we observe that the winter ASTD distribution rapidly shifts to the right; its average tends towards zero. Figure 17 shows the air mass ASTD histogram for the data recorded by weather ship CHARLIE in the Newfoundland Basin. Although CHARLIE is not very far from BRAVO, the distribution is almost centred around zero. Large negative ASTDs (below -6 °C) have disappeared and cases of positive ASTDs (stable conditions) are present.
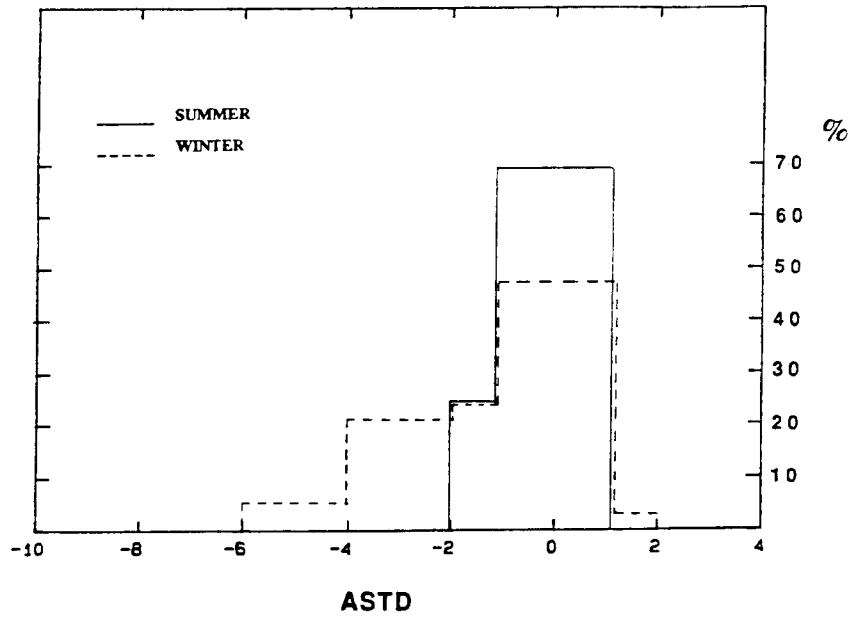
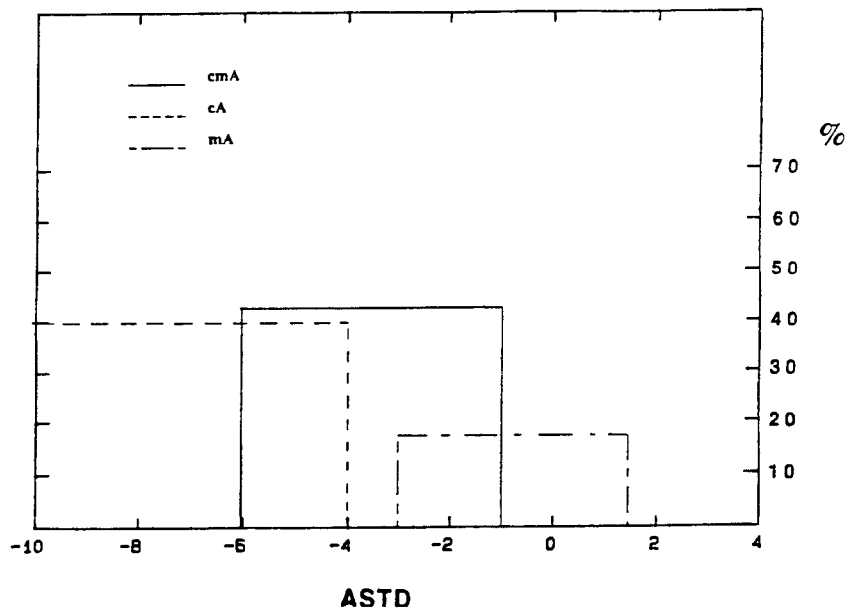FIGURE 15 - Simplified ASTD histograms for winter and summer in the Bermuda region

FIGURE 16 - ASTD distribution by air mass in the Labrador Basin in winter;
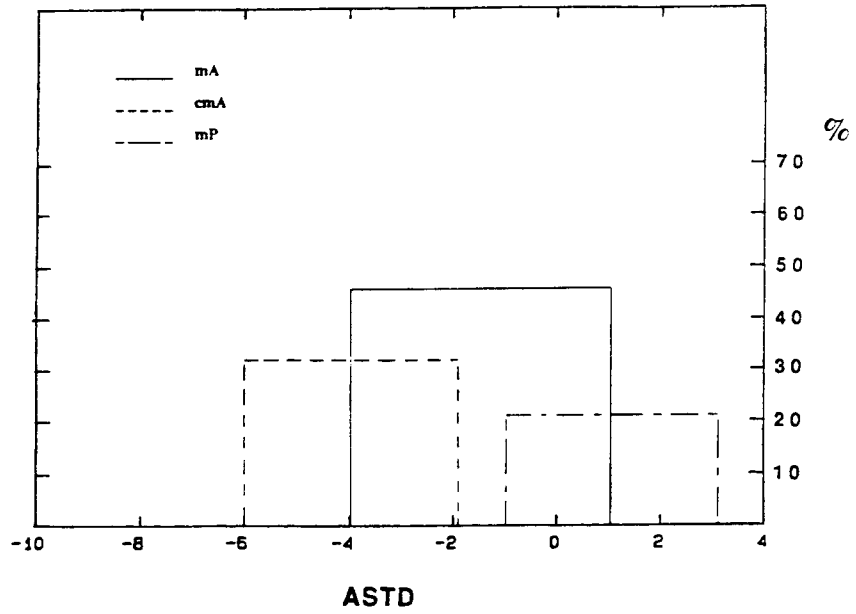each box represents 90% of the recorded ASTDs

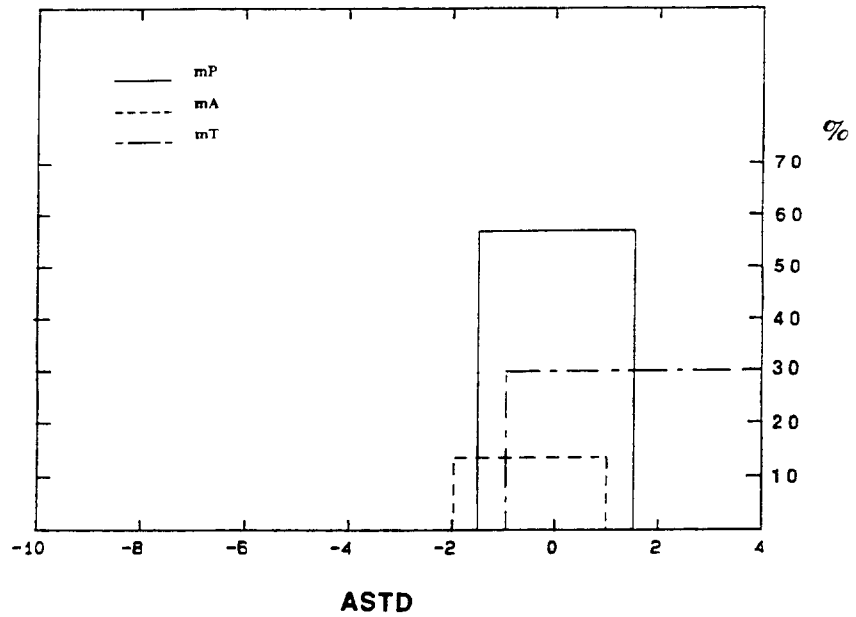FIGURE 17 -ASTD distribution by air mass in winter in the Newfoundland Basin

FIGURE 18 - ASTD distribution by air mass in summer in the Newfoundland Basin

During summer, as the weather warms up in the CANLANT region, highly negative ASTD conditions disappear and the occurrence of stable conditions (positive ASTD) increases and may become significant. In the Labrador Basin, the occurrence of positive ASTDs remains relatively low: 9% in summer, as opposed to 4 % in winter. However, in the Newfoundland Basin, it goes from 15% in winter to 20% in summer. During summer in the Newfoundland Basin, we notice that, when an mT air mass prevails, a positive ASTD is observed 37% of the time. As shown in Fig. 18, this air mass occurs 30% of the time.

It was shown in Chapter 4.0 that a positive ASTD may substantially extend the MIVR and thereby potentially extend the detection range. However, positive ASTD conditions are likely to be accompanied by fog or haze which cause a strong absorption of the IR radiation. Using correlated statistics on ASTD versus visibility under stable conditions (positive ASTD), one can attempt to estimate the proportion of events where visibility is such that it could counter the potential extended detection range. As a first approximation, assuming that, optimistically, in the IR, visibility above the sea may be about 4 times better than in the visible, we find that, in the Newfoundland Basin, the extended detection range would be nullified under 20 to 30% of the stable conditions.

6.0 DISCUSSION

Using ray tracing, IR refractivity effects in the marine boundary layer have been investigated on a representative spectrum of meteorological profiles for a sensor located 22 m above sea level. The refractivity phenomena that may affect detection performances have

been identified as: maximum inter-vision range (MIVR) variation, generation of an angular error and potential mirage formation. Our analysis focuses on these phenomena.

First, the calculation of air refractivity in the IR was investigated in order to find a valid expression which gives refractivity in relation to standard meteorological parameters. A parametric analysis showed that in the region of the IR window free of significant resonances, the refractivity gradient mainly depends on the temperature profile; the water vapour contribution is, in general, more than an order of magnitude lower than that of the temperature.

A preliminary analysis of the refractivity effects was first performed under the hypothesis of a linearly varying atmosphere. This provided basic indications on the variation of the maximum inter-vision range (MIVR) and the angular errors. For the main analysis, IR refractivity profiles were modelled to agree with the basic principles of the marine boundary layer theory, while being consistent with the microwave profiles as established in the NAAWS project. Although this has not been done in this study, this modelling approach allows us to make correlations between refractivity effects in the IR and at microwaves, since both analyses are based on equivalent assumptions. However, this profile modelling technique reduces the analysis in the IR to a restricted class of meteorological conditions. A significant limitation is that the wind effect (which affects air stability) is not fully taken into account in the temperature profile modelling.

The marine boundary layer theory prescribes a logarithmic variation of temperature, and thus refractivity, with respect to the elevation near the sea surface. A dominant characteristic of these profiles is that they present very strong gradients quite close to the

surface. Air refractivity mostly changes in the first metres above the surface, and thus it affects propagation mainly at very low elevations. However - and this is a major uncertainty in the analysis - one reasonably expects that, actually, propagation in a thin layer adjacent to the surface will normally be highly perturbed by the presence of aerosols and by potentially strong evaporation. Furthermore, the effect of waves is not accounted in the profile modelling; a calm sea is assumed. As contended in Ref. 8, it is not unreasonable to believe that a lower portion of the profile could be virtually "washed out" by waves under certain conditions. In order to obtain indications about the impact of all these unincorporated surface phenomena, we have assessed, at various stages of the analysis, the effects caused when cancelling out the energy that propagates in thin surface layers of varied thickness; these hypothetical surface layers were called "absorbing surface layers".

Further to the main uncertainties discussed above, it must be pointed out that the refractivity functions used represent temporal and spatial mean profiles. Actually, the profiles may significantly vary in a relatively short period of time and, also, with respect to the range. One should then expect increasing uncertainty as the range increases in the cases under study. Therefore, in general, one should be very careful when drawing conclusions on the numerical results obtained from this ray-tracing analysis. It has been carried out to provide indications on the potential effects of refractivity and to provide preliminary data on their magnitude in relation to weather conditions.

In discussing the refractivity effects, it is convenient to group the weather conditions into two classes of stability: unstable conditions characterized by a negative air-sea temperature difference (ASTD), and stable conditions characterized by a positive ASTD. Under unstable conditions, the numerical results show a reduction of the MIVR that

may reach up to 13 km (under strongly unstable conditions) for a sea-skimming target flying 5 m above sea level. More precisely, the MIVR goes from about 26 km (geometrical horizon) to about 13 km under adverse conditions. However, we noticed that when the MIVR is reduced, the intensity of the radiation increases near the MIVR, compared with an homogeneous condition, and therefore, the probability of detection should be improved when the target reaches the MIVR. Simple tests have indicated that under strongly unstable conditions, the effect of refractivity on sea-skimming targets should not be altered much by the perturbing near-surface phenomena.

Under stable conditions, extended MIVRs are theoretically predicted. Under these conditions, however, the MIVR proves to be very dependent upon the propagation very close to the sea surface. Ray tracing shows that the energy that reaches sea-skimming targets beyond the horizon has to skim the earth very closely over an appreciable distance. Eliminating the propagation in the first metre (simulating a 1-m absorbing surface layer), we obtained MIVR gains that could reach 10 to 15 km with respect to the geometrical horizon. However, when extended MIVR occurs, from the horizon and beyond, the power density of the radiation decreases much more rapidly than in $1/r^2$. The detection range should then be much less than the MIVR predictions.

Comparing these results with those obtained when considering linear refractivity profiles, we observe that under unstable conditions, the computed MIVRs are roughly the same for high ASTDs. A notable difference exists however for weak ASTDs. Under stable conditions, the results are fairly different. The linear profile gives a much sharper increase of the MIVR. This is mainly due to the assumed absorbing surface layer.

The angular error obtained using logarithmic profiles is not very appreciable. It would be less than 1 mrad under unstable conditions and, although it is expected to be higher under stable conditions, it should not exceed 1 mrad by much. However, according to the results obtained using linear profiles, the angular error proves to be highly sensitive to profile modelling; linear profiles generate angular errors about 5 times greater than those obtained using logarithmic profiles. Consequently, errors greater than 1 mrad would not be impossible.

Under unstable conditions, logarithmic profiles generate a zone, which extends from the MIVR, where more than one ray hit a point target. This phenomenon, called mirage, would appear at the sensor either as a double image, one above the other, or as a major distortion (stretching) of the expected image. When a double image is distinctly apparent, the lower image should appear as if it was reflected by the sea surface. The ray tracing showed that the angular separation between the two point images should not exceed 1 mrad by much even under extreme conditions. Therefore, for real targets, a distortion of the image is expected rather than a distinct double image. The width of a mirage zone is unlikely to exceed 3 km and should not appreciably vary with respect to the environmental conditions. The mirage effect proves to be very vulnerable to the near-surface perturbations since the lower image is produced by rays that skim the earth very closely. Considering a 2-m absorbing surface layer (as opposed to the 1-m layer), the mirage zone was found to be shortened to about 1 km at most. Ray crossing that causes mirage is generated by the variation of refractivity gradient, the second derivative of the refractivity function. One then expects that, as the assumed temporal and spatial invariability of the function is highly sensitive to the atmospheric perturbations, the probabilities of a clear and persistent mirage are very low.

Considering two North Atlantic regions, the CANLANT and Bermuda regions, we examined meteorological statistics to obtain information about the occurrence of conditions that can produce noticeable refractivity effects in the IR in relation to the geographical locations and the time of year. Highly negative ASTDs are observed in winter and become more frequent and greater as one moves north. High occurrence (40% in winter) of very strong decrease of temperature (< -4) is measured in the Labrador Basin; ASTDs as large as -10 °C are encountered. These conditions, as discussed above, should significantly shorten the MIVR and would present a high risk of mirage. The occurrence of highly negative ASTDs decreases rapidly when moving south. In the Newfoundland Basin, which is adjacent to the Labrador Basin, the probability of very negative ASTDs is significantly lowered; ASTDs greater than -6 are improbable.

Significantly positive ASTDs (stable conditions), which can produce extended MIVRs are logically likely to be encountered either in warm regions (such as those close to the equator) or in northern regions during summer. The statistics reveal that in the CANLANT region the occurrence of stable conditions is low in general, except in some subregions. In the Newfoundland Basin, stable conditions are recorded about 20% of the time in summer. We have shown that these conditions produce extended MIVRs. However, these conditions are likely to be accompanied by low visibility as a highly positive ASTD facilitates the formation of fog. Based on correlated statistics between ASTD and visibility, we have estimated that, in the Newfoundland Basin, bad visibility would nullify the advantage of a predicted extended MIVR in about 25% of the stable conditions. Consequently, neglecting the decrease of power density that lowers the detectability (when the MIVR is greater than the horizon), an over-the-horizon detectability

would be possible about 15% of the time during summer in that region. The surface aerosols and the presence of a strong evaporation (likely to occur in these conditions) would tend to lower that frequency of occurrence.

Moving slightly to the south, the conditions become mainly neutral or near-neutral (ASTD $\approx$ 0) most of the time and thereby, chances of significant refractivity effects can be discarded; in the Bermuda region, ASTDs below -4 and above +2 ^{o}C are very improbable.

In this report, we have focussed on the refractivity effects produced in the boundary layer at the sea surface. However, as emphasized in another study (Ref. 1), the IR propagation can also be affected by the presence of an elevated temperature-inversion layer. In the microwave region, this condition is responsible for the formation of a class of duct known as surface-based duct. As shown in Ref. 1, at optical wavelengths, when both the target and the sensor are in or near the inversion layer, a significant image distortion can occur. Although, on a world average basis, the occurrence of a strong and low-altitude layer (near the sensor) is known to be low, some regions show a high occurrence of inversion layers. For instance, it is more than 45% in the Persian Gulf. It would therefore be of interest to assess the potential impact of refractivity on shipborne detection under these conditions.

Finally, it must be emphasized that the analysis presented in this report is only a preliminary study of refractivity effects. The phenomena are actually much more complex than what is represented here and the unaccounted factors may invalidate the results presented here under some circumstances. However, we made an effort to obtain, through simple tests, elements of information on the possible contribution of some of these factors

such as surface aerosols and sea state. Should the results shown here not be very reliable

concerning the actual effects of refractivity, they at least provide a rough estimate of the

limits of their impact on sensor performance.

7.0 CONCLUSION

In the study of the complementarity of electro-optical and radar systems aboard

ships, the issue of the impact of air refractivity at optical wavelengths was raised. An

investigation of the IR refractivity effects in the marine boundary layer was then

undertaken. The results of a preliminary analysis were presented in this report.

The calculation of air refractivity was first investigated and an expression that gives

the refractivity as a function of standard meteorological parameters was developed. It was

shown that the refractivity phenomena are mainly determined by the variation of air

temperature. Consequently, the analyzed refractivity effects were presented in relation to

the air-sea temperature difference (ASTD), which is a standard meteorological

measurement.

Air refractivity may significantly affect the maximum inter-vision range (MIVR),

which is an absolute limit of detection range. According to our analysis, strongly unstable

conditions (characterized by a negative ASTD) can decrease the MIVR up to 10 km (in the

worst case). Meteorological statistics reveal that unstable conditions are quite frequent in

the Northern Atlantic (e. g. 40% in the CANLANT region). Conversely, stable conditions

(characterized by a positive ASTD) can potentially lead to beyond-the-horizon detection

ranges. Although the occurrence of stable conditions is low in most regions, it can be significant in northern regions during summer (e.g. 20% during summer in the Newfoundland Basin). However, stable conditions are often accompanied by low visibility (more than 25% of the time) which nullifies the extended MIVR. Furthermore, extended MIVRs prove to be highly sensitive to the near-surface perturbations, such as the extinction due to aerosols and surface evaporation and the sea state effects, which could prevent any potential extended detection range.

Air refractivity can also cause an angular error. Because of refractivity, the actual target position differs from the one observed. However, our results show that this error should normally not exceed 1 mrad. However, since the angular error depends highly on the shape of the refractivity profile, it could exceed that value under certain conditions.

Mirage, or multiple-image formation, can also be created by air refractivity. Under unstable conditions, the logarithmic variation of refractivity can produce a mirage over a short distance (3 km at the most) when the target reaches the MIVR. As extended MIVRs, mirages are very vulnerable to perturbations near the surface. Under most conditions, strong image distortion (e.g. image stretching) is expected rather than a distinct double image.

The numerical results presented in this report should not be used as reliable predictions of the refractivity effects with respect to meteorological conditions. They nevertheless indicate that refractivity could play a nonnegligible role in the performance of shipborne sensors depending on the conditions.

Further analyses have to be carried out in order to obtain more reliable predictions about the refractivity effects in relation to environmental conditions. Conditions of high ASTD (positive and negative) must be emphasized as they could cause the most significant effects. A more accurate model must be used to describe the refractivity profile and the surface perturbations (such as sea state effects and the aerosol extinction) must be rigorously taken into account. Moreover, it is essential to validate analytical results with experimental measurements.

8.0 ACKNOWLEDGEMENTS

9.0 REFERENCES

1. Feinberg, R., Hitney, H. V. and Hughes, H. G., "Marine Boundary Layer Refractive Effects in the Infrared", NOSC TN 555, NOSC, San Diego, CA, 1978.

2. Smith, E.K. and Weintraub, S., "The Constants in the Equation for Atmospheric Refractive Index at Radio Frequencies", Proc. IRE 41, 1953, pp. 1035-7.

3. Allen, K. C. and Liebe, H. J., "Tropospheric Absorption and Dispersion of Millimetre and Submillimetre Waves", IEEE Trans. on Ant. and Prop., Vol. AP-31, No. 1, 1983.

4. Slater, J. C. and Frank, N. H., "Electromagnetism", McGraw-Hill, New York, NY, 1969.

5. Born, M. and Wolf, E., "Principles of Optics", Fifth Edition, Pergamon Press, Oxford, England, 1975.

6. Goody, M. R., "Atmospheric Radiation; Theoretical Basis I", Oxford, Clarendon Press, 1964.

7. Edlén, B., "The Dispersion of Standard Air", J. Opt. Soc. Am., Vol. 43, No. 5, pp. 339-343, May 1953.

8. Larsen, R. and Sharp, I. E., "Oversea Propagation of Infra-Red Radiation", UK Study on Infrared Propagation Over the Sea - Contract Number SWN 41A/0054, GEC-Marconi Limited, England, 1988.

9. Hill, R. J., Clifford, S. F. and Lawrence, R. S., "Refractive-Index and Absorption Fluctuations in the Infrared Caused by Temperature, Humidity, and Pressure Fluctuations", J. Opt. Soc. Am., Vol. 70, No. 10, pp. 1192-1205, 1980.

10. Hill, R. J. and Lawrence, R. S., "Refractive Index of Water Vapour in Infrared Windows", Infrared Phys., Vol. 26, No. 6, pp. 371-376, 1986.

11. Richter, J. H. and Hitney, H. V., "The Effects of Atmospheric Refractivity on Microwave Propagation", Proceedings of the International Workshop on Atmospheric Water Vapor, Held in Vail, Colorado, 1979, Academic Press, New York, NY, pp. 203-218, 1980.

12. Jeske, H., "The State of Radar-Range Prediction Over the Sea", Tropospheric Radio Wave Propagation, AGARD CP-70 (Part II), pp. 50-1 - 50-6, 1971.

13. Rotheram, B. A., "Radiowave Propagation in the Evaporation Duct", Marconi Review, First Quarter, 1974.

14. Hitney, H. V., "Evaporation Duct Effects on Low-Altitude Propagation Guidelines for the NATO AAW System Project", NAAWS TDP TASK 3-1-18, 1988.

15. Brocks, K. and Krügermeyer, L. K., "The Hydrodynamic Roughness of the Sea Surface", Studies in Physical Oceanography, Vol. 1, Gordon and Breach Science Publication, pp. 75-92, 1972.

16. Montgomery, R. B., "Observations of Vertical Humidity Distributions above the Ocean Surface and Their Relation to Evaporation", Papers in Physical Oceanography and Meteorology, MIT and Woods Hole Oceanographic Institution, Vol. VII, No. 4, 1940.

17. Picard, G., Dion, D. and Pindam, M., "The Complementarity of Electro-Optical and Radar Systems for Ship Defence: The Meteorological Module", DREV R-4401/86, May 1986, UNCLASSIFIED

18. Kline, M. and Kay, I., "Electromagnetic Theory and Geometrical Optics", Krieger Publishing, Huntington, NY, 1979.

19. Dion, D., "Méthode des rayons avec calcul d'intensité appliquée à la propagation anormale", CRDV R-4407/86, juin 1986, SANS CLASSIFICATION

20. Kerr, D. E., "Propagation of Short Waves", MIT, Radiation Laboratory Series, McGraw-Hill, New York, NY, 1951.

21. Cross, R.K., Picard, G. and Pindam, M., "Summary Report on the Characterization of the Environmental Conditions for NATO Maritime Regions and Derivation of a Special Subset of Environmental Profiles for the NAAWS Project", DREV R-4534/89, January 1989, UNCLASSIFIED

22. Blanchard, A., "A Method for Computing the Radar Intensity Attenuation due to Geometric Spreading in a Medium with a Variable Index of Refraction", DREV M-2680/84, May 1984, UNCLASSIFIED